THESIS FOR THE DEGREE OF MASTER OF SCIENCE

Computational study of the atomic structure of grain boundaries in solid oxides

ANDERS LINDMAN

CHALMERS

Department of Applied Physics
CHALMERS UNIVERSITY OF TECHNOLOGY
Gothenburg, Sweden 2011

Computational study of the atomic structure of grain boundaries in solid oxides

ANDERS LINDMAN

Department of Applied Physics
Chalmers University of Technology
SE-412 96 Göteborg
Sweden
Telephone + 46 (0)31-772 1000

Printed at Chalmers Reproservice
Göteborg, Sweden 2011

Abstract

$BaZrO_3$ is a perovskite oxide that is a good candidate for an intermediate temperature proton conductor in SOFC, because it is chemically stable and has high bulk proton conductivity. However, the total conductivity of the material is low due to high proton resistance at the grain boundaries. Theories suggest that this is caused by oxygen vacancy migration to these boundaries.

The aim of this project was to study oxygen vacancy segregation in $[\bar{1}10]$ symmetric tilt grain boundaries of $BaZrO_3$. A semi-empirical interatomic potential has been used to study the boundaries since first-principles simulations are too computationally heavy for most of them. A study of two simple grain boundaries was conducted with both methods to determine the transferability of the potential. The study suggested that the semi-empirical approach predicts the structure and energy of the boundaries in a reasonably accurate manner.

The structures of eight different grain boundaries with reasonable grain boundary energy were found using the interatomic potential. The oxygen vacancy segregation of these boundaries was then investigated. The results showed that the preferred vacancy positions were close to the boundary planes for each grain boundary and the minimum segregation energies were in the range [-1.86,-0.83]eV, which suggests that oxygen vacancy migration to the boundaries will occur.

Polarizability was also introduced to the simulations through use of the shell model. These simulations predicted different energies but similar structures, and the same segregation ordering as the simulations without polarizability.

Contents

1 Introduction 1

2 Barium zirconate 3

3 Atomistic modelling 7
- 3.1 First-principles 7
- 3.2 Semi-empirical 8
- 3.3 Boundary conditions 10

4 Structure minimization 11

5 Grain boundary structures 13
- 5.1 Grain boundary orientation 14
- 5.2 Termination 14
- 5.3 Supercell size 15

6 Results 19
- 6.1 Method comparison 19
- 6.2 Grain boundaries 24

7 Discussion 31

8 Conclusion 35

Acknowledgements 37

Bibliography 39

Chapter 1

Introduction

Fuel cells have very high efficiency and are considered to be a good clean alternative to the combustion engine since they do not need fossil fuels to operate. There exists many different types of fuel cells. The main principle of them is the same but they differ when it comes to properties such as the fuel, the operating temperature and the mobile ions for ionic conduction. One of them is the Solid Oxide Fuel Cell, SOFC, which is interesting due to three of its attributes. Both H_2 and CO can be used as fuel, it operates at high temperatures (500-1000 °C) which means that high reaction rates can be obtained without expensive catalysts, and it consists only of solid parts [1].

The conventional SOFC contains an oxygen ion conducting electrolyte and the ceramic used for this purpose is mainly yttria-stabilized zirconia, YSZ. YSZ has high ionic conductivity, $>10^{-2}$ S/cm, but only at high operating temperatures, 800-1000 °C, and low electron conductivity [1]. Such high temperatures are not preferable in practical applications since more time and energy is required to reach them, heat sealing becomes more difficult and the life time of the fuel cell could be reduced due to thermal stress [2, 3].

Since there is an interest in lowering the operating temperature to the intermediate range, 500-750 °C, other types of ionic conductors have been investigated and it has been found that proton conducting perovskite oxides exhibit high conductivity, $\sim 10^{-2}$ S/cm, at these temperatures [4]. However, there are problems with perovskite oxides as proton conductors. Two of the main features of a good electrolyte, high ionic conductivity and high chemical stability, seem to counteract each other in these materials. For example, $BaCeO_3$ and $SrCeO_3$ has a high proton conductivity but reacts with CO_2 which makes them chemically unstable [4]. It has been found that the low conductivity found in some of the perovskite oxides is caused by high resistance at the grain boundaries [5]. This is the case for the $BaZrO_3$ where the bulk conductivity is a few orders of magnitude higher than the grain boundary conductivity. [5, 6]. However, $BaZrO_3$, which is very chemically stable [3, 7], has a high bulk proton conductivity, $\sim 10^{-2}$ S/cm [5], that is of the same order as the best proton conducting perovskite oxides. If the grain boundary resistance could be reduced in some way then $BaZrO_3$ would be a very suitable material for electrolytes in SOFC.

The purpose of this project was to investigate the structure and properties of grain boundaries in $BaZrO_3$ using a semi-empirical interatomic potential, in order to get a better understanding of the low proton conductivity. Previous computational studies of grain boundaries in perovskite oxides have been made using Density Functional Theory, DFT [8, 9]. DFT is an accurate simulation technique but computationally heavy, and is therefor limited to small system sizes. Most of the grain boundaries considered in this project needs larger system sizes in order to be modelled in a proper manner, and that is why a semi-empirical interatomic potential has been used instead of DFT.

The project consisted of two main parts. In the first part, both DFT and the interatomic potential were used to determine the grain boundary energy and structure for grain boundary orientations which can be modelled using small system sizes. This was done in order to determine the accuracy of the interatomic potential. In the second part of the project, the structures of eight different grain boundary orientations were determined using the interatomic potential. The oxygen vacancy segregation was then investigated for these grain boundaries in order to verify theories that suggest that the low grain boundary conductivity is caused by vacancies at the boundaries.

The structure of the report is as follows. The next chapter gives a description of the structure of $BaZrO_3$ as well as a summary of previous studies of this material. Chapter 3 and 4 presents the theoretical background to the simulation methods used within this project. Chapter 5 gives a description of grain boundaries in general as well as the specific ones used within this project. The results of the simulations are given in chapter 6 and these results are then discussed in chapter 7. Finally, a conclusion of the project is given in chapter 8.

Chapter 2

Barium zirconate

Barium zirconate is a perovskite oxide with the formula $BaZrO_3$. It has a cubic perovskite structure, which is shown in Fig. 2.1. Previous studies have shown that barium zirconate has a high (grain interior) proton conductivity, $\sim 10^{-2}$ S/cm, at intermediate temperature (500-700 C°) [10] and is very mechanically and chemically stable [3, 7]. Some other perovskite oxides, such as $BaCeO_3$, also exhibits high proton conductivity but reacts with CO_2, which makes it less chemically stable than barium zirconate [3]. These properties suggest that barium zirconate is a good candidate as an electrolyte in SOFCs. However, there is one major drawback with barium zirconate as a proton conductor. The proton conductivity in grain boundaries is much lower than in the grain interior, with a factor between $10^{-4} - 10^{-2}$ depending on oxygen partial pressure, temperature and dopant concentration [11, 6]. Experiments has shown that an increase in the average grain size, meaning fewer grain boundaries per volume unit, gives a higher proton conductivity, which also suggest that the grain boundaries reduce the proton conductivity [3].

There are two main theories for the low proton conductivity at the grain boundaries. One of them suggest that it is because the grain boundaries are charged. The effect is described by the space charge model which suggests that the grain boundary can be seen as a grain boundary core with a space charge layer on each side. The charged grain boundary is caused by vacancy migration to the core since it is assumed that it is more energetically favorable for the vacancies to be there. The vacancies are charged which means that the accumulation of vacancies at the boundary core results in a charged core. The area surrounding the core, i.e. the space charge layers, will experience a depletion of vacancies due to electrostatic repulsion which will make these regions charged as well, but with opposite sign compared to the grain boundary core [12]. For $BaZrO_3$, and other proton conducting

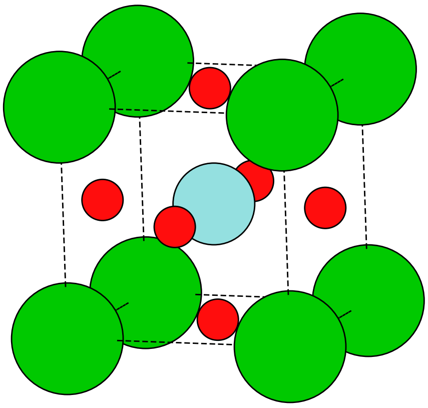

Figure 2.1: The cubic perovskite structure of Barium zirconate. The green, gray and red colored atoms represents Ba, Zr and O atoms respectively.

oxides as well, the mobile vacancies are oxygen vacancies. The vacancies have a charge of 2+ which results in a positively charged grain boundary core and negatively charged space charge layers. Since the protons have a positive charge there will be a lower concentration of protons in the space charge layers which reduces the conductivity [6]. The space charge model has also been used to explain the effect of the grain boundaries on the conductivity in other types of ionic conductors, such as oxide ion conductors [13].

The other theory suggests that it is due to the change in distance between oxygen ions at the boundary. The protons move through the material by jumping between oxygen ions and the activation energy for these jumps are strongly related to the distance between the oxygen ions. At the boundary the lattice structure changes which changes the oxygen-oxygen distance and the activation energy for these jumps can increase [5]. A high concentration of vacancies would also increase the oxygen-oxygen distance.

When used as a proton conductor barium zirconate is doped with 3+ ions such as yttrium or indium. The reason for doping is to increase the number of mobile protons in the material which are needed for proton conduction. When Zr^{4+} ions are replaced by 3+ ions the system becomes charged. To maintain a charge neutral system, oxygen vacancies are formed in order to compensate for negative charge caused by the doping. If water vapor is introduced into the doped system, water molecules get absorbed into the oxygen vacancies and mobile protons are created [14]. When barium zirconate is doped it has the formula $BaZr_{1-\alpha}R_{\alpha}O_{3-\beta}$ where R is the dopant ion, α is the dopant ion concentration and β is the concentration of oxygen vacancies [3, 4, 7, 15, 10, 11, 16]. In this study however, pure $BaZrO_3$ is considered since the purpose of this project is to investigate if vacancy migration to grain boundaries is a general feature of the material. The effect of the dopant ions is neglected and the charge difference is compensated by a charged background [17].

Chapter 3

Atomistic modelling

Atomistic modelling is an approach to describe the structure of an atomic system with the use of an interatomic potential. If one consider a system with N atoms, then the interatomic potential V, which represents the configurational energy, of this system is given by the positions of these atoms according to

$$V = V(\boldsymbol{R}_1,\boldsymbol{R}_2,...,\boldsymbol{R}_{N-1},\boldsymbol{R}_N). \tag{3.1}$$

To use the exact form of this potential is not possible since it is to computationally heavy, so it needs to be approximated in some way [18]. Two ways in doing so is the first-principles approach and the semi-empirical approach which are described in section 3.1 and 3.2 respectively.

3.1 First-principles

The first-principles approach means that one simplifies the original problem using approximations based on theory rather than experimental data. Such an approximation that is always considered is the Born-Oppenheimer approximation which states that because the nuclei are much heavier than the electrons, they are considered fixed from the electrons' point of view. One can then solve the Schrödinger equation for the electronic structure which gives an expression for the potential $V(\boldsymbol{R}_1,...,\boldsymbol{R}_N)$. Two methods for doing first-principles calculations are Hartree-Fock theory and density functional theory, DFT [19].

No first-principles calculations have been conducted within this thesis work. However, results from DFT calculations have been used to determine the accuracy of the semi-empirical potential, which is described in the next section. The approximations made within these DFT calculations predict the bulk lattice parameter of $BaZrO_3$ to 4.25 Å [20] which is fairly close to the experimental value of 4.19 Å [21].

3.2 Semi-empirical

The principle of the semi-empirical approach is that one assumes that interactions between atoms can be described with a potential. This potential has some material specific parameters that one try to fit with experimental or first-principles data, so that the potential mimics the properties of the desired system. The form of the semi-empirical potential differs depending on the type of the problem. The most simple one is the pair potential which can be used for systems where atoms do not share electrons, such as noble gases and ionic systems. If one wants to model more complex interactions, such as covalent or metallic bonds, then more complex potentials are needed, such as many-body potentials [22]. However, since $BaZrO_3$ is the material considered in this project, the atomic systems are of ionic character and thus a pair potential can be been used. When a pair potential is used, Eq. 3.1 can be written as

$$V = \sum_{i=1}^{N} \sum_{j>i}^{N} U_{ij}(R_{ij}), \tag{3.2}$$

where $U_{ij}(R_{ij})$ is the pair potential and $R_{ij} = |\boldsymbol{R}_i - \boldsymbol{R}_j|$, which is the distance between atom i and j.

The specific pair potential that has been used in this thesis work has the form

$$U_{ij}(R_{ij}) = A_{ij} e^{-R_{ij}/\rho_{ij}} - \frac{C_{ij}}{R_{ij}^6} + \frac{q_i q_j}{R_{ij}}, \tag{3.3}$$

where A_{ij}, ρ_{ij} and C_{ij} are constants which are dependent on the type of ions and q_i and q_j is the formal charge of the ions. The first term on the right-hand side represents Pauli repulsion, which is an effect that causes nearby ions to repell each other because their electron clouds overlap [18]. The second term is van der Waals interaction, which is a weak force that attracts ions to each other due to dipole fluctuations [18]. This description of these two types of interaction together is called a Buckingham potential. The third term on the right-hand side represents the Coulomb interaction, which is the electrostatic interaction between ions. The parametrization of the Buckingham potential for $BaZrO_3$ used within this project is from [23] and the values of these parameters are given in Table 3.1. This parametrization

Table 3.1: Buckingham potential parameters for $BaZrO_3$. [23]

Interaction	A(eV)	ρ (Å)	C (eV Å^6)
$Ba^{2+} \cdots Ba^{2+}$	0.000	0.0000	0.000
$Ba^{2+} \cdots Zr^{4+}$	0.000	0.0000	0.000
$Ba^{2+} \cdots O^{2-}$	931.700	0.3949	0.000
$Zr^{4+} \cdots Zr^{4+}$	0.000	0.0000	0.000
$Zr^{4+} \cdots O^{2-}$	985.869	0.3760	0.000
$O^{2-} \cdots O^{2-}$	22764.300	0.1490	27.890

is fitted to empirical data so that the bulk lattice parameter of $BaZrO_3$ is 4.19 Å [23] which coincides with the experimental value of 4.19 Å [21].

To save time when performing simulations one often limits the reach of the short-range part of the potential. This can be done since at a certain length, based on the form of the potential, these interactions are approximately zero and can therefor be neglected. This length, which is often referred to as the cut-off radius, was set to 6 Å for all the simulations within this project.

The Coulomb interactions can not be limited in the same way as the short-range interactions and to calculate them in an efficient manner requires other methods. The method used within this project is the Ewald sum technique. The concept of this method is that Coulomb interactions are divided into a short-range part and a long-range part. The short-range part is treated in the same way as the other short-range interactions while the long-range interactions are calculated in reciprocal space [17].

In the semi-empirical approach with the pair potential discussed so far, each ion is represented by a sphere with a mass and a fixed charge. However, in reality, the charge of the ions are often polarized in some way which is a feature that this description does not possess. Polarizability can be introduced by taking use of the shell model [24]. The principle of the shell model is that the ion is represented as a core and a massless shell that are connected through a harmonic spring. The core can be seen as the nucleus and the inner electrons, while the shell can be seen as the valence electrons. The sum of the core and shell charges is equal to the formal charge of the ion. The harmonic spring contributes to the energy according to

$$V(r) = \frac{1}{2}k_s r^2, \tag{3.4}$$

where r is the distance between the centers of the core and the shell and k_s is the spring constant which depends on the type of ion. The values of

Table 3.2: Shell model parameters for $BaZrO_3$. [23]

Ion	q_s (e)	k_s (eV/Å^2)
Ba^{2+}	1.460	14.800
Zr^{4+}	1.350	269.617
O^{2-}	-2.077	27.300

k_s and the shell charge q_s for the different ions in $BaZrO_3$ that were used within this thesis work are given in Table 3.2.

3.3 Boundary conditions

Since it is not possible to have an infinite system when conducting computer simulations, boundaries occur which means that one has to specify the boundary conditions. When conducting atomistic modelling of the interior of a material, the most common to use is periodic boundary conditions, since the size of the simulated system is often much smaller than real system. However, when using such conditions together with the interatomic potential described in the previous section the system should be large enough so that atoms do not interact with themselves over short ranges. If all system dimensions are at least twice as long as the reach of short-range potential then the energy due to these interactions is only a sum over all these interactions [19]. The atoms will still interact with themselves over long ranges but this is corrected for when using the Ewald sum technique [17]. As mentioned in the previous section, the length of the short-range potential was set to 6 Å which means supercell of the simulated system should at least have a length of 12 Å along each axis.

Chapter 4

Structure minimization

In the previous chapter, methods of modelling the atomic structure were described. However, in order to find the desired structure one needs some type of search algorithm. The sought-for structures within this project are grain boundaries with low energy, which results in an energy minimization problem. The methods in the previous chapter are very suitable for energy minimization since it is possible to find an expression for the gradient $\nabla V(\boldsymbol{R}_1,...,\boldsymbol{R}_N)$.

There is one large difficulty with this minimization and that is that the sought-for structures are grain boundaries which are not global but local minima. The global minimum of the system is the bulk structure which is already known. The grain boundary energy also varies between different boundaries so the difficulty lies in finding the local minimum within each grain boundary orientation.

The search algorithm used to find the grain boundary structures within this project is a combination of the conjugate gradient method and molecular dynamics, MD, where these two methods were applied in alternation. The conjugate gradient method is a line minimization algorithm where the search directions, which in a way are based on the gradients of the function, are conjugates [25]. This method was the optimizing part of the search algorithm. However, the conjugate gradient method can only proceed in directions which lowers the energy. To get a broader search area and to avoid getting stuck in high energy local minima one needs an additional search method and this is where MD comes in. MD is a classical method of describing the motion of atoms by making use of Newton's equation of motion

$$\frac{\mathrm{d}^2\boldsymbol{R}_i}{\mathrm{d}t^2} = \frac{\boldsymbol{F}_i(\boldsymbol{R}_1,...,\boldsymbol{R}_N)}{m_i},\ \ i = 1,...,N, \tag{4.1}$$

where the force $\boldsymbol{F}_i(\boldsymbol{R}_1,...,\boldsymbol{R}_N)$ is related to the potential $V(\boldsymbol{R}_1,...,\boldsymbol{R}_N)$

through the relation

$$\boldsymbol{F}_i(\boldsymbol{R}_1,...,\boldsymbol{R}_N) = -\nabla_i V(\boldsymbol{R}_1,...,\boldsymbol{R}_N). \tag{4.2}$$

The velocities of the atoms are controlled by the temperature through the equipartition principle [26]. The temperature was reduced during the simulations in order to narrow down the MD search area. During the simulations it was also found that the conjugate gradient method was very sensitive to the initial structures, resulting in non-physical configurations or even terminating the simulation. This problem was solved by always starting the simulations with some steps of MD.

When conducting MD simulations one have to choose within which type of ensemble the simulation will occur. An ensemble is a set of states which a system can be in while obeying some criteria, such as a fixed number of particles, conserving energy or keeping a constant temperature. Ensembles are introduced by modifying Newton's equation in different ways [26]. The choice of ensembles for the conducted simulations is given later on in chapter 6.

The software DL_POLY has been used to perform the simulations within this project. This software can perform both MD simulations and structure optimization. It can handle various types of potentials as well as different types of statistical ensembles. It is specifically written for parallelization in order to take full advantage of the processing power within a computer cluster [17]. The simulations within this work have been conducted on the computer cluster Beda, which is ran by C^{3}SE [27].

Chapter 5

Grain boundary structures

If one have two grains with the same orientation one can create boundaries by translation and rotation of one of them. By rotation one can create two types of boundaries, twist and tilt boundaries. A twist boundary occurs when one grain is rotated around the axis perpendicular to grain interface. A tilt boundary occurs when rotating one of the grains around an axis parallel to the grain interface. These two types of grain boundaries can be seen in Fig. 5.1. Using these degrees of freedom one can create a lot of different types of grain boundaries, however those associated with a high interfacial energy are in most situations less likely to appear.

The grain boundaries used within this thesis are described in the following sections. The grain orientations are treated in section 5.1 and the grain boundary termination in section 5.2. The choice of supercells are described in section 5.3.

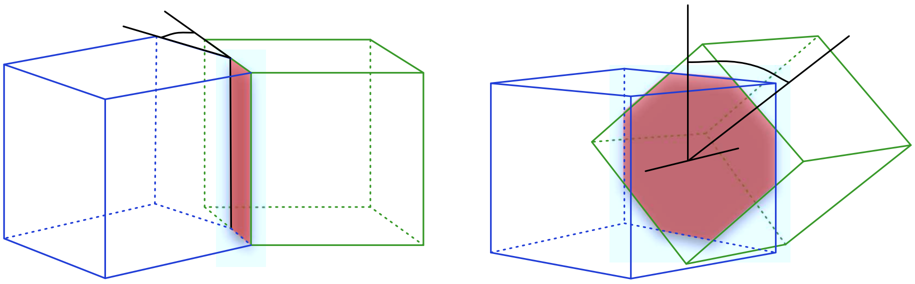

(a) Tilt boundary.

(b) Twist boundary.

Figure 5.1: A geometrical representation of twist and tilt grain boundaries. The red area in the figures is the grain boundary interface.

5.1 Grain boundary orientation

The type of grain boundaries considered within this project is a special case of tilt boundaries, namely a symmetric tilt boundary. This is a tilt boundary where the two grains are symmetric around the interface. A symmetric tilt grain boundary is characterized by two vectors. The first vector represents the axis perpendicular to the interface and the second one represents the axis which the grains are rotated around, the tilt axis. For example, the $(111)[\bar{1}10]$ grain boundary is a boundary where (1,1,1) is the boundary plane and $[\bar{1}10]$ is the direction which the grains are rotated around.

The boundaries considered in this project all have the same tilt axis which is $[\bar{1}10]$. What distinguish them from one another is the axis perpendicular to the interface. The boundaries that are considered are the ones with the boundary planes $(1,1,i)$, where $i = 1,...,8$. There are two reasons for this choice of boundaries. The first one is that the $(111)[\bar{1}10]$ and $(112)[\bar{1}10]$ grain boundaries have been studied with DFT which can used to determine how accurate the potential is, which is done later on in chapter 6. The second reason is that since all of these grain boundaries are of the same type, i.e. they have the same tilt axis, the results will be more comparable. The grain boundaries are chosen to be stoichiometric, since a neutral system is preferred when using periodic boundary conditions [19]. Determining the grain boundary energy also becomes more difficult if the system is nonstoichiometric because one then needs to know the chemical potential of individual atoms [28].

5.2 Termination

Depending on the crystal structure of materials different types of planes in the same direction might occur. In the $(1,1,i)$ directions of $BaZrO_3$, which is of cubic perovskite structure (see chapter 2), there exists two types of planes which repeat after each other. This means that different boundaries can occur for the same directions depending on which plane that is present at the interface. The choice of plane is called the termination of the boundary.

The termination of the boundaries within this project was chosen so that Ba and O atoms always are present in boundary plane. In some cases Zr atoms are present as well due to the grain boundary orientation. The reason for always having BaO-termination is that the BaO-terminated $(111)[\bar{1}10]$ grain boundary has a grain boundary energy of $0.036\,\mathrm{eV/Å^2}$, while the Zr-terminated $(111)[\bar{1}10]$ grain boundary has $0.172\,\mathrm{eV/Å^2}$. This is almost five

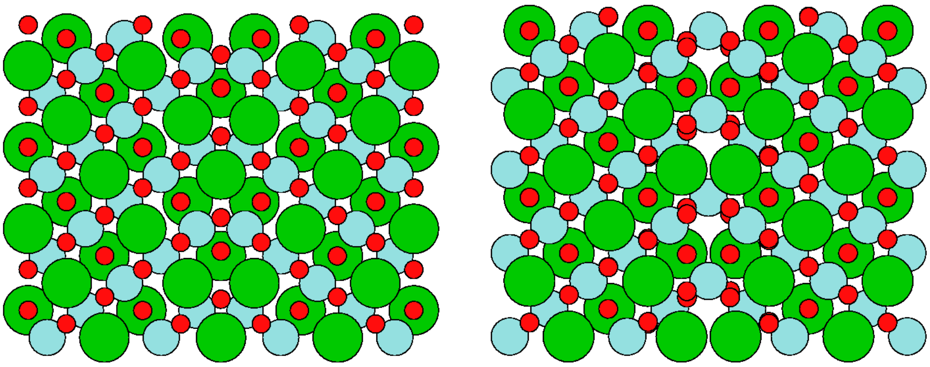

(a) BaO-termination. (b) Zr-termination.

Figure 5.2: Two possible terminations of the (111)[$\bar{1}$10] grain boundary. The structures are relaxed.

times as much which suggest that BaO-termination is more likely to occur. These two termination types can be seen in Fig. 5.2.

5.3 Supercell size

When dealing with grain boundaries the supercell needs to be quite large. This is due to that since the two grains have different orientation, periodic boundary conditions gives rise to a periodic set of grain boundaries in the system. When investigating properties of the grain boundary such as energy, expansion and segregation, the distance between two boundaries in the system must be long enough so that the boundaries do not interact.

In order to determine the minimum distance needed to avoid interactions between the boundaries, the segregation energy of oxygen vacancies in a large cell was determined. Segregation energy is the energy difference between a grain boundary vacancy and a bulk vacancy, and it is described in greater detail in section 6.2. The reason for choosing this quantity over others such as grain boundary energy and expansion was that the cell size could be fixed for all simulations which reduces the errors caused by periodic boundary conditions. If the segregation energy converges when moving from the boundary then the structure is of bulk character, which means that the interactions between the boundaries are small and can be neglected. The considered supercell was an (111)[$\bar{1}$10] grain boundary with the dimensions 20.6 × 17.8 × 121.3 Å. These dimensions gives a distance between the boundaries in this cell of 60.7 Å.

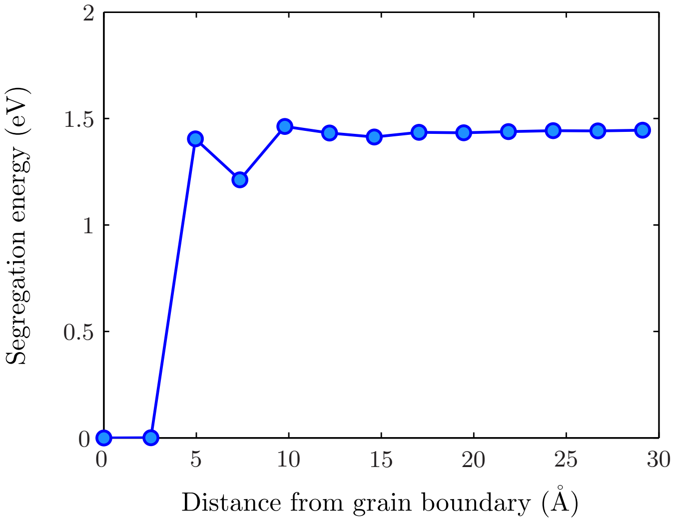

Figure 5.3: The segregation energy of the (111)[$\bar{1}$10] grain boundary. The vacancy in the grain boundary plane is used as the reference point. The supercell dimensions are 20.6 × 17.8 × 121.3 Å.

The vacancy segregation energies calculated with this large supercell are shown in Fig. 5.3. Here one can see that the energy converges for vacancies at the distance of 12-13 Å from the boundary plane which gives that the distance between the boundaries should at least be 26 Å. This means that the minimum length of the supercell perpendicular to the grain boundary needed in order to get non interacting grain boundaries is 52 Å.

To calculate some properties of the grain boundaries, such as energy and expansion, one need a bulk reference system. In order to prevent computational errors, e.g. due to boundary conditions, it is important that both the grain boundary and bulk supercells have the same amount of ions, and similar shape and size. Due to these criteria, the number of ions for each grain boundary system have been chosen so that its unrelaxed structure has the same supercell dimensions as the unrelaxed bulk system with the same orientation. The dimensions for these unrelaxed structures as well as the number of molecular units in them are given in Table 5.1.

Table 5.1: The unrelaxed structure dimensions and the number of molecular units for $[\bar{1}10]$ tilt grain boundaries supercells of $BaZrO_3$. The last dimension is the one perpendicular to the grain boundary.

GB	Dimensions (Å)	#$BaZrO_3$
(111)	$20.5 \times 17.8 \times 58.1$	288
(112)	$14.5 \times 17.8 \times 61.6$	216
(113)	$19.7 \times 17.8 \times 83.4$	396
(114)	$25.1 \times 17.8 \times 71.1$	432
(115)	$30.8 \times 17.8 \times 87.1$	648
(116)	$18.3 \times 17.8 \times 77.5$	342
(117)	$42.3 \times 17.8 \times 59.9$	612
(118)	$24.1 \times 17.8 \times 68.1$	396

Chapter 6

Results

This chapter contains the results from the different simulations made within this project. As described in chapter 3, the semi-empirical interatomic potential describes the bulk structure of $BaZrO_3$ in a correct manner. However, it is not certain that it will model grain boundaries with the same accuracy. In order to determine how well it does that, a comparison has been made between interatomic potential calculations and DFT. DFT is a first-principles method and therefor more accurate. The considered grain boundaries are the $(111)[\bar{1}10]$ and $(112)[\bar{1}10]$ grain boundaries. The comparison of these methods is given in section 6.1.

The purpose of the simulations described in section 6.2 was to investigate if vacancy segregation is a general grain boundary behavior. If so, it might be the reason for the high proton resistance at the boundaries. This was done by first finding the correct structures of eight different grain boundaries and then calculating the segregation energy for them, using the interatomic potential both with and without the shell model.

Not all the simulations described in this chapter were done by the author. All the DFT simulations as well as the interatomic potential simulations of the $(112)[\bar{1}10]$ grain boundary were conducted by members of the same research group at Chalmers.

6.1 Method comparison

When doing grain boundary simulations, the length of the direction perpendicular to the grain boundary should be long in order to reduce the interaction between the grain boundaries. However, DFT simulations are limited to a small supercell size. The $(111)[\bar{1}10]$ and $(112)[\bar{1}10]$ grain boundaries have a short period in the directions parallel to the boundary and can be modelled in a correct manner with DFT. These two boundaries have therefor been used in this comparison. The number of atoms in the supercells used for for the DFT simulations was 180 for both grain boundaries, which is 36 $BaZrO_3$ molecular units. The number of molecules in the supercells used for the potential simulations are given in Table 5.1 in the previous chapter.

As mentioned in chapter 4, one has to decide which ensemble to use when conducting MD simulations. When searching for bulk and grain boundary structures the NST ensemble was used. When using this ensemble the number of particles is fixed, and temperature and pressure is kept constant, through a Nosé-Hoover thermo- and barostat [26], while the cell is allowed to change size and shape, i.e. volume [17]. The ability to change shape and size is needed because the initial unrelaxed structure is only an assumption of how the relaxed structure would look like.

The first grain boundary property considered in the comparison was the grain boundary energy, σ_{GB}. σ_{GB} is the energy increase per area unit of grain boundary interface compared to the bulk system, and is defined as

$$\sigma_{GB} = \frac{E_{GB} - E_{Bulk}}{2A}, \tag{6.1}$$

where E_{GB} and E_{bulk} are the energies of the grain boundary and bulk supercells respectively and A is the area of the grain boundary interface. Since periodic boundary conditions are used each supercell contains two grain boundaries, hence the prefactor 1/2. σ_{GB} for the two boundaries are given in Table 6.1. Here one can see that the different methods give similar results for the $(111)[\bar{1}10]$-grain boundary, while they differ more for the $(112)[\bar{1}10]$-grain boundary, especially DFT and the shell model.

The energy alone is not enough to compare the methods, since it does not tell anything about the grain boundary structure. A way to characterize the structure is to determine the grain boundary expansion δ_{GB}. δ_{GB} is defined as the increase of the grain boundary supercell compared to the bulk supercell in the direction perpendicular to the grain boundary interface, divided with a factor 2 since there are two grain boundaries in the cell. The calculated values of δ_{GB} for the two grain boundaries are given in Table 6.1. The results suggest that the $(111)[\bar{1}10]$ grain boundary is modelled in a similar way using the different methods while there are larger differences for $(112)[\bar{1}10]$ grain boundary. However, DFT and the shell model gives very similar results for both boundaries.

The grain boundary expansion gives a crude characterization of the structure, so in order to get more detailed information of how the atoms are positioned one can look at the interplanar spacing deviation, Δd_{ij}. Δd_{ij}

Table 6.1: The grain boundary energy and grain boundary expansion of the (111)[$\bar{1}$10] and (112)[$\bar{1}$10] grain boundaries calculated with both DFT and an inter atomic potential, with and without the shell model.

GB	σ_{GB} (eV/Å^2)			δ_{GB} (Å)		
	DFT	Pot.	Pot. w. shell	DFT	Pot.	Pot. w. shell
(111)	0.030	0.036	0.034	0.20	0.13	0.24
(112)	0.059	0.052	0.044	0.46	0.28	0.49

is a measure of how the distance between planes in the grain boundary cell deviates from that of the bulk cell. Since the planes vary for different grain boundary orientations, the expression for Δd_{ij} differs between grain boundaries.

In the (111) direction there are two different planes, one with Ba and O atoms and one with Zr atoms. The expression of Δd_{ij} for the (111)[$\bar{1}$10] grain boundary is therefore

$$\Delta d_{ij} = |[(\mathrm{Ba}_j^z + \mathrm{O}_j^z)/2] - \mathrm{Zr}_i^z| - d_{bulk}, \tag{6.2}$$

where d_{bulk} is the interplanar spacing between (111) planes in bulk. Ba_j^z, O_j^z and Zr_i^z is the mean z-position of Ba, O and Zr atoms respectively and the lower index represents the plane, where the grain boundary plane is defined as the 0th plane. The z-direction is the axis perpendicular to the grain boundary [8].

In the (112) direction there are also two types of planes but of a different character. One of the planes consists of Ba, Zr and O atoms while the other consists only of O atoms. The expression for the (112)[$\bar{1}$10]-grain boundary is therefore

$$\Delta d_{ij} = |[(\mathrm{Ba}_j^z + \mathrm{Zr}_j^z + \mathrm{O}_j^z)/3] - \mathrm{O}_i^z| - d_{bulk}, \tag{6.3}$$

where all the terms have the same meaning as in the previous equation except for d_{bulk} which now is the interplanar spacing between bulk (112) planes instead. The interplanar spacing deviation for the two grain boundaries can be seen in Figs. 6.1 and 6.2 respectively. Here one can see that the different methods yields similar results, especially for the (111)[$\bar{1}$10] grain boundary.

An even more detailed characterization of the structure can be made by determining the rumpling, η_i. η_i is a measure of how distorted the Ba and O atoms in the same plane are and is defined as

$$\eta_i = |\mathrm{Ba}_i^z - GB^z| - |\mathrm{O}_i^z - GB^z| \tag{6.4}$$

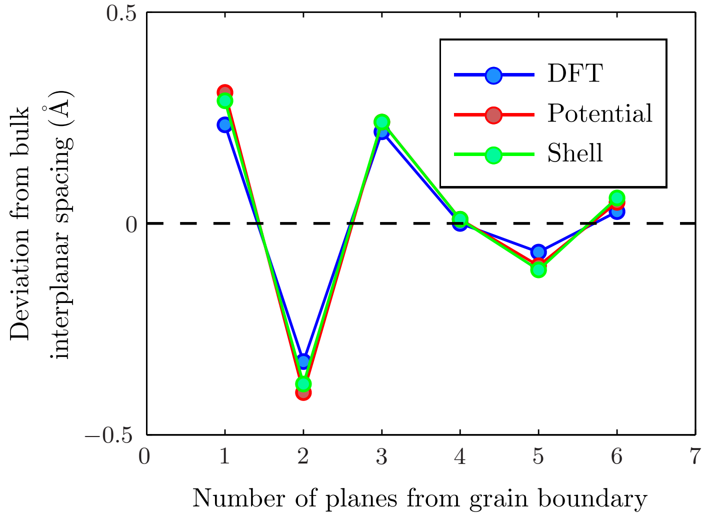

Figure 6.1: The interplanar spacing deviation of the (111)[$\bar{1}$10] grain boundary.

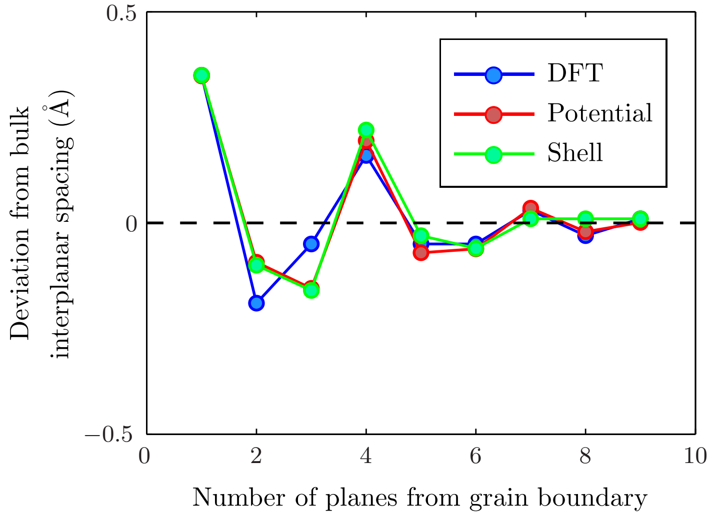

Figure 6.2: The interplanar spacing deviation of the (112)[$\bar{1}$10] grain boundary.

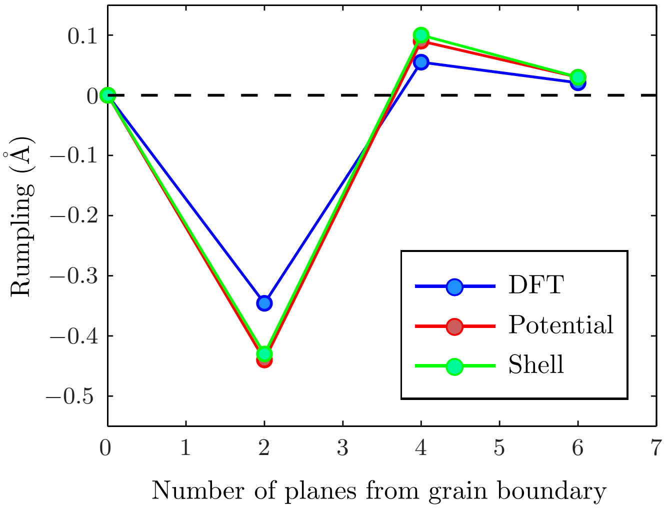

Figure 6.3: The rumpling of the (111)[$\bar{1}$10] grain boundary.

where Ba_i^z and O_i^z has the same meaning as in Eqs. 6.2 and 6.3 and GB^z is the z-position of the grain boundary plane [8]. The rumpling for the two boundaries are given in Figs. 6.3 and 6.4. The rumpling for the (111)[$\bar{1}$10] grain boundary differs a little between DFT and interatomic potential calculations but follows the same trend. For the (112)[$\bar{1}$10] grain boundary the results differ more, especially between the calculations with and without the shell model.

To summarize the results from this comparison one can say that the interatomic potential calculations yields similar results to those obtained with DFT, especially for the (111)[$\bar{1}$10] grain boundary. The use of polarization through the shell model increases the accuracy of the interatomic potential, especially when it comes to the structural properties.

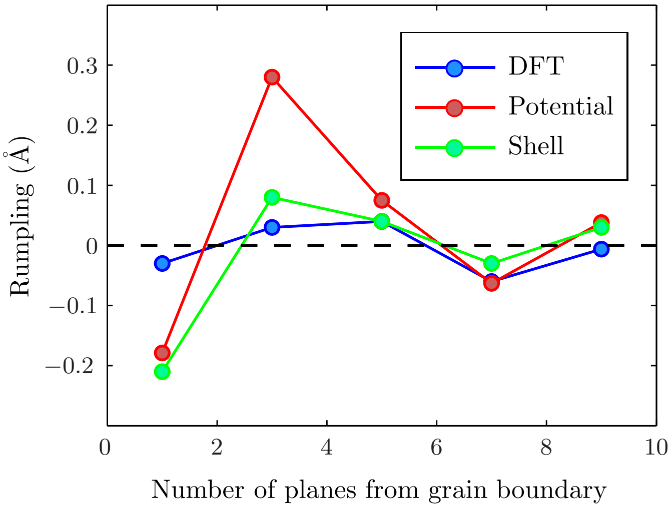

Figure 6.4: The rumpling of the (112)[$\bar{1}$10] grain boundary.

6.2 Grain boundaries

In order to determine if oxygen vacancy migration occurs one first needs a set of grain boundaries. The grain boundaries that are considered are $(11i)[\bar{1}10]$ symmetric tilt boundaries, with $i = 1,...,8$, and they are described in more detail in chapter 5. Before one can determine if oxygen vacancies segregates to these boundaries, one has to find the correct structure of the boundaries as well as make sure that they are physically possible (not too high grain boundary energy and expansion). Using the same procedure as described in the previous section the grain boundary energy and expansion was determined for these boundaries. The values of these properties are given in Table 6.2. The structure of these grain boundaries can be seen in Figs. 6.5-6.12. In these figures one can see, except for the (111) grain boundary, that the grain boundaries are no longer symmetric around the grain boundary plane. The grain orientations are still the same but one of the grains have been translated during the relaxation. All these translations have occurred in the direction which is parallel to the grain boundary plane and perpendicular to the tilt axis $[\bar{1}10]$, and they are given in Table 6.3.

In Table 6.2 one can also see that there is a difference in grain boundary energy of 0.002-0.011 eV/Å^2 between simulations with and without the shell model. However, when comparing the grain boundary expansion of the same grain boundary obtained with the two methods one can see that they are very similar.

To find out if oxygen vacancies would segregate to the grain boundary

Table 6.2: The grain boundary energy σ_{GB}, expansion δ_{GB} and minimum segregation energy E_s of $[\bar{1}10]$ tilt grain boundaries for $BaZrO_3$ calculated both with and without the shell model. The grain boundaries are defined by the axis perpendicular to grain boundary interface.

GB	σ_{GB} (eV/Å^2)		δ_{GB} (Å)		E_s (eV)	
	No shell	Shell	No shell	Shell	No shell	Shell
(111)	0.036	0.034	0.13	0.24	-1.37	-1.05
(112)	0.052	0.044	0.28	0.49	-0.83	-0.54
(113)	0.076	0.067	1.68	1.68	-1.56	-1.20
(114)	0.078	0.068	1.24	1.21	-1.35	-1.10
(115)	0.092	0.081	1.90	1.90	-1.48	-1.11
(116)	0.097	0.086	1.76	1.43	-1.79	-1.58
(117)	0.106	0.094	1.88	1.88	-1.86	-1.74
(118)	0.106	0.095	1.60	1.47	-1.75	-1.74

within these structures, one could calculate the segregation energy for different vacancy positions. The segregation energy of a vacancy i, $E_s(i)$, is defined as

$$E_s(i) = E_v(i) - E_v(\text{bulk}), \tag{6.5}$$

where $E_v(i)$ is the vacancy energy for the considered vacancy and $E_v(\text{bulk})$ is the vacancy energy for a vacancy in a bulk system. The bulk system in these calculation is the region between the two grain boundaries in the grain boundary supercell which is positioned with equal distance to both boundaries. This is a valid assumption according to section 5.3. Before one can calculate $E_s(i)$ one need to determine $E_v(i)$. The vacancy energy is defined as the energy difference between the total energy of a relaxed supercell with one vacancy and the total energy of a relaxed supercell without vacancies. When a vacancy is introduced the system becomes charged and a background charge of opposite sign has therefor been used in order to compensate for that. This will affect the vacancy energy. However, all vacancy energies will be changed in the same way which means that the background charge will not alter the segregation energy.

As mentioned in the previous section, the NST ensembles was used when determining the structures. However, when performing these oxygen vacancy simulations, the NVT ensemble was used instead. This ensemble keeps the temperature constant, through a Nosé-Hoover thermostat [26], as well as the cell size and shape [17]. The reason for keeping the cell fixed is that it is preferable to have the same cell dimensions when determining the segregation energy. The vacancy together with the periodic bound-

Table 6.3: The translation of the relaxed grain boundaries along the axis which is parallel to the grain boundary plane and perpendicular to the tilt axis. The translation is defined in such a way so that the grain to the left of the boundary is considered to be fixed while the grain on the right-hand side is translated in a downward manner. The structure is periodic and a translation of 1 equal to that of no translation at all. The period of the structures in this direction is given in the second column.

GB	Translation	GB period (Å)
(111)	0	10.27
(112)	0.66	7.35
(113)	0.89	19.66
(114)	0.78	12.57
(115)	0.92	30.80
(116)	0.84	18.27
(117)	0.92	42.33
(118)	0.88	24.08

ary conditions creates a lattice of vacancies, which, when comparing two simulations, can give rise to errors if these vacancy lattices have different structures.

The vacancy with lowest segregation energy is the most preferable position for a vacancy and it is to that position vacancies will migrate. The values of $\min_i E_s(i)$ for each of the eight different boundaries are given in Table 6.2. In Figs. 6.5-6.12 one can see the positions of the oxygen ions which, if removed, gives rise to the vacancies with the lowest segregation energies. These ions are marked as blue. In all grain boundaries except the (112), the different blue oxygen ions gives rise to the same vacancy. This means that the initial positions of the vacancies are different but the structure minimization rearranges the ions of the system so that the relaxed position of the vacancy is the same for all these vacancies. In the case of the (112) grain boundary there are actually two different relaxed vacancy positions with the lowest segregation energy. In Table 6.2 one can also see that the segregation energy of the shell model simulations and the ordinary ones differ. However, the positions of these vacancies are the approximately same in both simulations. The values in Table 6.2 as well as the marked positions in Figs. 6.5-6.12 suggest that the vacancies will segregate to the grain boundary.

To summarize the results in this section one can say that oxygen vacancies segregates to the grain boundaries for all the considered grain boundary

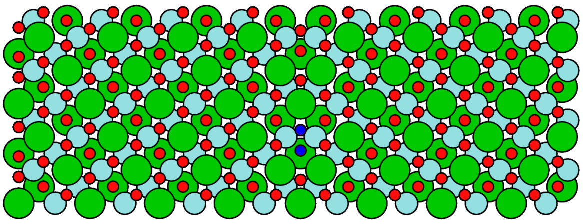

Figure 6.5: The relaxed structure of the (111)[$\bar{1}$10] grain boundary. The direction to the right of paper is [111] and the direction out of paper is [$\bar{1}$10]. The blue atoms mark the oxygen sites which creates the vacancies with lowest energy. The segregation energy is -1.37/-1.05 eV calculated without/with the shell model.

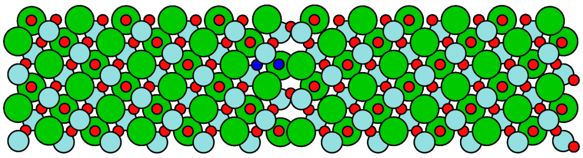

Figure 6.6: The relaxed structure of the (112)[$\bar{1}$10] grain boundary. The direction to the right of paper is [112] and the direction out of paper is [$\bar{1}$10]. The blue atoms mark the oxygen sites which creates the vacancies with lowest energy. The segregation energy is -0.83/-0.54 eV calculated without/with the shell model.

orientations. When using the shell model one get different energies but the structures and energy ordering of the vacancies remains approximately the same.

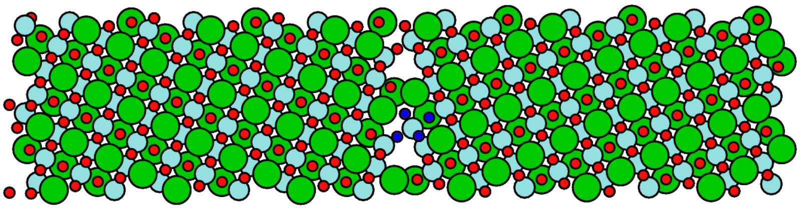

Figure 6.7: The relaxed structure of the (113)[$\bar{1}$10] grain boundary. The direction to the right of paper is [113] and the direction out of paper is [$\bar{1}$10]. The blue atoms mark the oxygen sites which creates the vacancies with lowest energy. The segregation energy is -1.56/-1.20 eV calculated without/with the shell model.

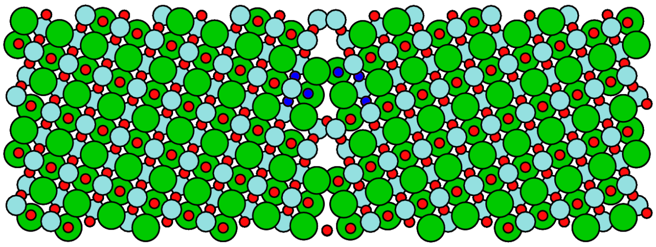

Figure 6.8: The relaxed structure of the (114)[$\bar{1}$10] grain boundary. The direction to the right of paper is [114] and the direction out of paper is [$\bar{1}$10]. The blue atoms mark the oxygen sites which creates the vacancies with lowest energy. The segregation energy is -1.35/-1.10 eV calculated without/with the shell model.

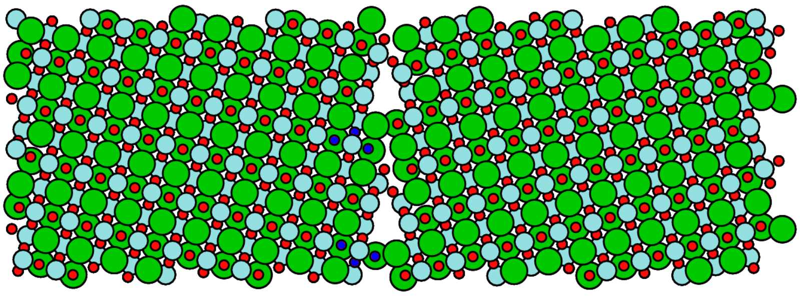

Figure 6.9: The relaxed structure of the (115)[$\bar{1}$10] grain boundary. The direction to the right of paper is [115] and the direction out of paper is [$\bar{1}$10]. The blue atoms mark the oxygen sites which creates the vacancies with lowest energy. The segregation energy is -1.48/-1.11 eV calculated without/with the shell model.

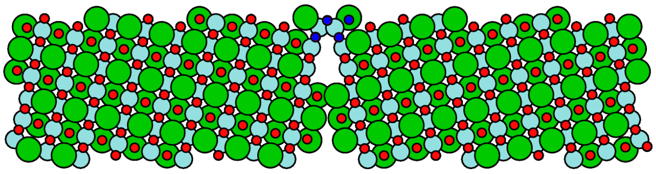

Figure 6.10: The relaxed structure of the (116)[$\bar{1}$10] grain boundary. The direction to the right of paper is [116] and the direction out of paper is [$\bar{1}$10]. The blue atoms mark the oxygen sites which creates the vacancies with lowest energy. The segregation energy is -1.79/-1.58 eV calculated without/with the shell model.

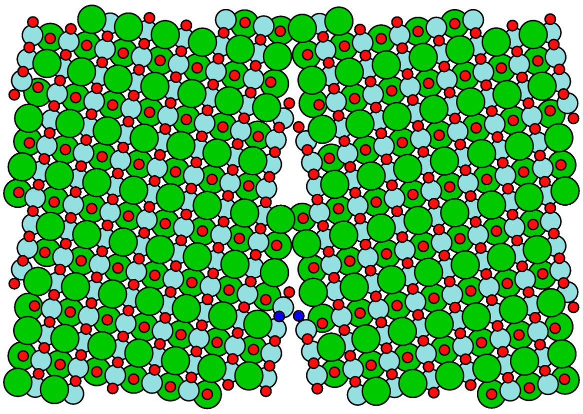

Figure 6.11: The relaxed structure of the (117)[$\bar{1}$10] grain boundary. The direction to the right of paper is [117] and the direction out of paper is [$\bar{1}$10]. The blue atoms mark the oxygen sites which creates the vacancies with lowest energy. The segregation energy is -1.86/-1.74 eV calculated without/with the shell model.

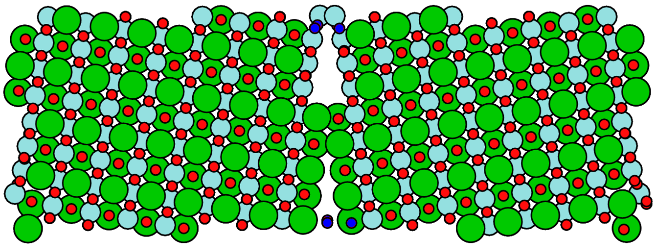

Figure 6.12: The relaxed structure of the (118)[$\bar{1}$10] grain boundary. The direction to the right of paper is [118] and the direction out of paper is [$\bar{1}$10]. The blue atoms mark the oxygen sites which creates the vacancies with lowest energy. The segregation energy is -1.75/-1.74 eV calculated without/with the shell model.

Chapter 7

Discussion

In the results from the comparison between the DFT and the interatomic potential simulations, described in the previous chapter, it was concluded that the interatomic potential could model the grain boundaries in an accurate manner, both with and without the shell. It is more precise for the (111) boundary but still good enough for the (112) boundary. For the (111) boundary the shell model was a little closer with a difference in grain boundary energy and expansion of only $0.004\,\mathrm{eV/Å^2}$ and $0.04\,\mathrm{Å}$ compared to DFT. The interplanar spacing deviation seen in Fig. 6.1 is also quite similar for all methods. The rumpling however, seen in Fig. 6.3, is not equally close but all curves follow the same trend.

In the case of the (112) boundary, there are larger differences between the different simulation techniques than for the (111) boundary but they are similar enough. The grain boundary energy and expansion are still close enough and the interplanar spacing deviation shown in Fig. 6.2 is also quite similar for all methods. The rumpling, shown in Fig. 6.4, is the property that varies most but the trend for all curves is almost the same.

A possible reason for that the (112) grain boundary results are not as good could be the lack of symmetry within the structure. When determining the parameters of the potential a bulk system was used. In the $BaZrO_3$ bulk, the structure is symmetric and all atoms of the same type has the same surrounding neighborhood, i.e. nucleus and electron distribution. However, at the grain boundaries this bulk symmetry is broken and the surrounding neighborhood of the atoms change. In the case of (111) boundary, the surroundings of the atoms changes at the boundary but not in a major way, which can be seen in Fig. 6.5. This means that the interatomic potential is still a quite accurate description. As can be seen in Fig. 6.6, the structure of the (112) boundary is anti-symmetric. This will cause the potential to be less accurate since in this case the surroundings of the atoms have changed a lot compared to the bulk structure.

One other thing, that probably does not affect the results that much but is still worth mentioning, is the fact that size of the supercells used for DFT and potential calculations differ quite a lot. Even though DFT simulations with different cell sizes has shown that the grain boundary energy and expansion has converged for the used cell size, identical systems are to be preferred when doing a comparison. However, to have the same cell size with both methods is not an option. The largest supercells used for the DFT simulations consist of about six times less ions than the smallest supercells used with the interatomic potential. The cpu time of these DFT simulations is about several hundred or even thousand hours. The cpu time of the shortest interatomic potential simulations is a few minutes, which makes these simulations $\sim 10^4$ times faster than DFT simulations. To simulate the larger systems within this project using DFT would be a matter of several hundred cpu days which is not possible. To reduces the systems used with the interatomic potential is not possible since then one would get self-interacting ions.

The simulations that are discussed above have also been conducted for the perovskite oxide $SrTiO_3$ [8]. Both DFT simulations as well as several different interatomic potential parametrizations were used, which all gave different grain boundary energies. However, both the interplanar spacing deviation and the rumpling obtained with these methods are very similar to the ones obtained for $BaZrO_3$ within this project.

In the second part of chapter 6 the structure for eight different grain boundary orientation was found. In Table 6.2 one can see the energy and expansion for these grain boundaries. Here one can see that the grain boundary energy increases when the index i in the orientation $(11i)$ increases. When i increases then the angle between the two grains decreases which results in that ions at the boundary becomes more closely packed. Ions that are too close to each other have a high energy due to electrostatic repulsion and the Pauli principle, and this is consistent with the grain boundary energies seen in Table 6.2. The grain boundary expansion is also increased for the low angle boundaries. Since the ions at the boundaries in the initial configurations are closely packed they want to increase the distance between each other which will result in a larger expansion. However, there is no relation found between i and the expansion as for the grain boundary energy.

The oxygen segregation energy given in Table 6.2 are high enough to ensure that the vacancies would segregate to that position. The positions of the low energy vacancy sites, which can be seen in Fig. 6.5-6.12, are all close to the grain boundary within each system. In the case of the

(112) boundary where there are two sites with the same low energy, both sites are close to the boundary. These results suggest that oxygen vacancy segregation to grain boundaries occur in $BaZrO_3$.

One has to keep in mind that since the number of ions in each system is fixed, the obtained boundaries for each orientation may not be most energetically favorable in a real system. In Figs. 6.7-6.12 one can see that there is an empty space at the grain boundary. These empty spaces could be filled by diffusion in the real system. If so, the grain boundary structure might change which then could result in that the position of the most favorable vacancy sites change. However, to investigate this is very time consuming since these empty spaces could be filled in many different ways and it is not obvious which ones that are most energetically favorable. This has therefore not been considered within this project.

As one can see in Table 6.2, when using the shell model the energy is different but the expansion is approximately the same. The energy ordering between different boundaries as well as between different vacancy positions is also the same with the shell model. These results together with the comparison suggest that shell model gives more accurate energies but almost no difference when it comes to structure. Since the shell model is much more computationally heavy, at least 10-20 times more, these results suggest that it is not preferable to only use this method. However, one could determine the structure without the shell model and from there use it to get a more accurate energy.

Chapter 8

Conclusion

According to the simulations done within this project one can say that the interatomic potential is accurate enough to model grain boundaries. To include polarization through the shell model gives a bit more accurate results but is much more time consuming. However, to combine simulations of both types is an advantageous approach. Furthermore, the results within this project suggest that oxygen vacancy segregation to the grain boundary is a feature shared by all grain boundary orientations. This gives indications to that the space charge model is a valid description of the low proton conductivity at the grain boundaries.

This thesis work only scratches the surface of $BaZrO_3$-based research and a lot more can be done within this field. There are a few topics that is a natural next step from this thesis work. When used as an proton conductor, $BaZrO_3$ is always doped with some kind of 3+ ions that replaces some of the Zr^{4+} ions [3, 4, 7, 15, 10, 11]. This will change the electron density at these sites. It is therefor of interest to perform simulations of the oxygen vacancy segregation as done in this project, but using doped $BaZrO_3$ instead. It is also of interest to investigate if the dopant ions segregate to the grain boundaries and affect the conductivity. A dopant ion that often is used in experiments and simulations is yttrium [7, 15, 10, 11, 6].

One could also do further investigations of pure $BaZrO_3$ to see if the results found within this project are transferable to other grain boundary types. A set of grain boundaries that could be suited for these simulations are [001] symmetric tilt grain boundaries. These grain boundary orientations have been used in previous studies of other perovskite oxides [9, 29] so a lot about the structures are already known.

Acknowledgements

First of all I would like thank my supervisor Göran Wahnström for giving me the opportunity to do this master's thesis and for guiding me through this project. I would also like to thank Edit Helgee for introducing me to DL_POLY and answering my questions as well as helping me with this report, and also Joakim Nyman for answering my questions. The simulations presented within this report that were not done by me were conducted by Edit and Joakim.

Further, I would like to thank Nils Jungenfelt, Björn Johansson and Emil Gustavsson for accompanying me on lunches and coffee brakes during this thesis work. Special thanks goes to Björn as well for helping me with some visual properties of this report.

At last I would like to thank Magdalena Kiszkiel for her everlasting support.

Bibliography

[1] Larminie, J. & Dicks, A. *Fuel Cell Systems Explained* (John Wiley & Son, 2003), 2nd edn.

[2] Ishihara, T. *Perovskite Oxide for Solid Oxide Fuel Cells* (Springer, 2009).

[3] Fabbri, E., Bi, L., Tanaka, H., Pergolesi, D. & Traversa, E. Chemical Stable Pr and Y Co-Doped Barium Zirconate Electrolytes with High Proton Conductivity for Intermediate-Temperature Solid Oxide Fuel Cells. *Advanced Functional Materials* **21**, 158–166 (2011).

[4] Kreuer, K. D. Proton-Conducting Oxides. *Annual Review of Materials Research* **33**, 333–359 (2003).

[5] Park, H. J., Kwak, C., Lee, K. H., Lee, S. M. & Lee, E. S. Interfacial protonic conduction in ceramics. *Journal of the European Ceramic Society* **29**, 2429–2437 (2009).

[6] Kjølseth, C. *et al.* Space–charge theory applied to the grain boundary impedance of proton conducting $BaZr_{0.9}Y_{0.1}O_{3-\delta}$. *Solid State Ionics* **181**, 268–275 (2010).

[7] Bohn, H. G. & Schober, T. Water vapor solubility and electrochemical characterization of the high temperature proton conductor $BaZr_{0.9}Y_{0.1}O_{2.95}$. *Solid State Ionics* **127**, 351–360 (2000).

[8] Benedek, N. A., Chua, A. L.-S., Elsässer, C., Sutton, A. P. & Finnis, M. W. Interatomic potentials for strontium titanate: An assessment of their transferability and comparison with density functional theory. *Physical Review B* **78**, 064110 (2008).

[9] Imaeda, M. *et al.* Atomic structure, electronic structure, and defect energetics in [001](310)$\Sigma 5$ grain boundaries of $SrTiO_3$ and $BaTiO_3$. *Physical Review B* **78**, 245320 (2008).

[10] Bohn, H. G. & Schober, T. Electrical Conductivity of the High-Temperature Proton Conductor $BaZr_{0.9}Y_{0.1}O_{2.95}$. *Journal of the American Ceramic Society* **83**, 768–772 (2000).

[11] Iguchi, F., Yamada, T., Sata, N., Tsurui, T. & Yugami, H. The influence of grain structures on the electrical conductivity of a $BaZr_{0.95}Y_{0.05}O_3$ proton conductor. *Solid State Ionics* **177**, 2381–2384 (2006).

[12] De Souza, R. A. The formation of equilibrium space-charge zones at grain boundaries in the perovskite oxide $SrTiO_3$. *Physical Chemistry Chemical Physics* **11**, 9939–9969 (2009).

[13] Guo, X. & Waser, R. Electrical properties of the grain boundaries of oxygen ion conductors: Acceptor-doped zirconia and ceria. *Progress in Materials Science* **51**, 151 – 210 (2006).

[14] Phair, J. & Badwal, S. Review of proton conductors for hydrogen separation. *Ionics* **12**, 103–115 (2006).

[15] Slade, R. C. T., Flint, S. D. & Singh, N. Investigation of protonic conduction in Yb- and Y-doped barium zirconates. *Solid State Ionics* **82**, 135–141 (1995).

[16] Iwahara, H., Asakura, Y., Katahira, K. & Tanaka, M. Prospect of hydrogen technology using proton-conducting ceramics. *Solid State Ionics* **168**, 299–310 (2004).

[17] Smith, W., Forester, T. R. & Todorov, I. T., *The DL_POLY_2 user manual*, (2010), http://www.cse.scitech.ac.uk/ccg/software/DL_POLY/.

[18] Kaxiras, E. *Atomic and Electronic Structure of Solids* (Camebridge University Press, 2003), 1st edn.

[19] Thijssen, J. M. *Computational Physics* (Camebridge University Press, 2007), 2nd edn.

[20] Sundell, P. G., Björketun, M. E. & Wahnström, G. Thermodynamics of doping and vacancy formation in $BaZrO_3$ perovskite oxide from density functional calculations. *Physical Review B* **73**, 104112 (2006).

[21] Pies, W., Weiss, A.: *e1388, XVII.2.1 Simple oxo-compounds of zirconium (oxozirconates).* Hellwege, K.-H., Hellwege, A.

M. (ed.). SpringerMaterials - The Landolt-Börnstein Database (http://www.springermaterials.com). DOI: 10.1007/10201569_35.

[22] Ercolessi, F., Parrinello, M. & Tosatti, E. Simulation of gold in the glue model. *Philosophical Magazine A* **58**, 213–226 (1988).

[23] Stokes, S. J. & Islam, M. S. Defect chemistry and proton-dopant association in $BaZrO_3$ and $BaPrO_3$. *Journal of Materials Chemistry* **20**, 6258–6264 (2010).

[24] Dick, B. G. & Overhauser, A. W. Theory of the Dielectric Constants of Alkali Halide Crystals. *Physical Review* **112**, 90–103 (1958).

[25] Press, W. H., Teukolsky, S. A., Vetterling, W. T. & Flannery, B. P. *Numerical Recipes: The Art of Scientific Computing* (Camebridge University Press, 2007), 3rd edn.

[26] Frenkel, D. & Smit, B. *Understanding Molecular Simulation: From Algorithms to Applications* (Academic Press, 2002), 2nd edn.

[27] C^3SE homepage, http://www.c3se.chalmers.se/index.php/Main_Page.

[28] Chua, A. L.-S., Benedek, N. A., Chen, L., Finnis, M. W. & Sutton, A. P. A genetic algorithm for predicting the structures of interfaces in multicomponent systems. *Nature Materials* **9**, 418–422 (2010).

[29] Oyama, T., Wada, N. & Takagi, H. Trapping of oxygen vacancy at grain boundary and its correlation with local atomic configuration and resultant excess energy in barium titanate: A systematic computational analysis. *Physical Review B* **82**, 134107 (2010).